Measuring air speed with a low-power MEMS ultrasonic anemometer via adaptive phase tracking

Ali Ghahramani, Megan Zhu, Richard J Przybyla, Michael P Andersen, Parson J Galicia, Therese E Peffer, Hui Zhang, Edward Arens

***Abstract*— Indoor air movement affects many functions of buildings, including ventilation and air quality, comfort and health of occupants, fire safety, and building energy use. Accurately measuring air movement has been difficult and expensive over extended periods of time, especially for velocities below 1 m/s. A new type of high frequency ultrasonic transceiver provides high sensitivity measurements and low cost through microelectromechanical systems (MEMS) manufacturing. However, at high frequencies, conventional ultrasonic signal processing algorithms function only over small ranges of ambient temperature and velocity. In this paper, we describe three algorithms that use the complex phase angle of an ultrasonic pulse to measure velocity and temperature over extended ranges of temperature and velocity. They employ heuristics to track the vibration cycle of the measured phase angle. These methods are applied in a pulse-based anemometer whose 176kHz MEMS transceivers both transmit and receive. In wind tunnel tests between 0-4 m/s, the tracking algorithm with a low-pass filter measured air speed with high sensitivity and accuracy (0.026 m/s mean absolute error). The ability to monitor to this accuracy with such low power draw and low cost is currently unprecedented in the industry.**

***Index Terms*— ultrasonic anemometry, pulsed ultrasound, complex phase angle, MEMS ultrasound, piezoelectric micromachined ultrasound transceivers.**

I. Introduction

MANY applications could benefit from a low cost and accurate measurement of low-speed air movement. Of the four variables (air and radiant temperatures, humidity, and air movement), air movement is most difficult and expensive to measure, so it is sparsely monitored. Deficiencies in monitoring and responsive control of air movement undermine systems providing indoor ventilation and air quality, impacting occupant comfort, health, and well-being. Accurate and real-time information about air movement would enable improved closed-loop feedback controllers for use in duct systems and for monitoring and alarms in indoor spaces where occupants or equipment such as computers require ventilation and cooling. They also have outdoor applications in agriculture and public health.

The term 'air movement' includes air speed (distance traveled by air in a period of time), air velocity (directional component of air speed in 3 dimensions), and air flow (volume of air passing in a period of time). Air movement is measured by different types of anemometers that take advantage of a flow's (1) mechanical forces, (2) induced pressure differences, (3) heat transfer properties of the fluid boundary layer, or (4) the time of travel across a known distance [1]. Mechanical anemometers generally involve rotating parts that are subject to friction, affecting calibration and the speed at which the device starts. Pressure differences measured across obstructions in the flow require sensitive pressure sensing, and often increase friction in the flow circuit. Electrically heated elements can be used to measure air speed in several ways: by rate of convective cooling, detecting the time for temperature pulses from a heated source upwind to be detected by a resistive element downwind, and by detection of the rate of vortex shedding by a bluff body element in the airflow. These each involve substantial power inputs and are susceptible to aging and fouling. Ultrasonic anemometers rely on the air flow changing the time required for sound to travel between two points. They have the potential to avoid many of the drawbacks of other anemometers.

Ultrasonic anemometers use high-frequency vibrating membranes functioning as both speaker and microphone to transmit and receive sonic waves traveling upwind and downwind. Airspeed is measured in in two ways: 1) a time-difference approach [2]-[6] that tracks and compares the envelope of arriving ultrasound pulses, and compares the upwind time-of-flight with the downwind time-of-flight, and 2) a phase-difference approach [7] that uses measurements of the phase of the received signals, arriving either in pulses or continuously. Phase-difference ultrasonic anemometers yield more accurate measurements than time-difference ultrasonic anemometers because phase angles are more sensitive to smaller changes in the time of flight caused by wind or temperature differences [8]. However, phase-difference methods described in the literature have lacked the ability to

Manuscript submitted on March 08 2019. This material is based upon work supported by 006521 California Energy Commission Electric Program Investment Change (EPIC), Grant Award #: EPC-14-013. (Corresponding author: Ali Ghahramani.)

A. Ghahramani, M. Zhu, P. J. Galicia, T. E. Peffer, H. Zhang, and E. Arens are with the Center of the Built Environment, University of California, Berkeley, CA, USA.

Michael P Andersen is with the Department of Electrical Engineering and Computer Science, University of California, Berkeley, CA, USA.

R. Przybyla is with the Chirp Microsystems, Berkeley, CA, USA.

http://dx.doi.org/10.1109/JSEN.2019.2920648
https://escholarship.org/uc/item/8kf1c11k

track the phase's cycle. These methods typically assume that airflow- and temperature-induced phase changes remain within a half-wave cycle, thus limiting the measurable velocity and temperature range of the anemometer [7]-[10]. Decreasing the ultrasound frequency decreases the airflow-induced phase difference and increases the half-cycle phase detection range [11], though at some cost in sensitivity. However, even for lower frequencies, the phase differences are prone to exceed half a cycle in typical air flows, especially during significant temperature changes.

To increase the detection range measured by phase-difference ultrasonic anemometers, we propose three new heuristic-based approaches to the phase-difference method. The goals are to increase the range of velocities measurable by the instrument, to automatically recover from the loss of phase cycle during rapid temperature changes, and to allow long-term operation with minimal energy demand. We specifically focus on a pulse-based approach. In contrast to a continuous wave approach, pulsed ultrasound time-separates extraneous echoes within a duct or room so that the received signals are not affected. Continuous wave methods also consume more power because the transmission power is typically many times larger than the receive power.

II. Fundamentals

In most ultrasonic anemometers, a pulse of high frequency sound is emitted from one transceiver and received by a second one, allowing the time of flight (TOF) of the transmission to be measured. The second transceiver then returns the pulse, allowing the influence of air movement along the path to be determined from the difference in the two transmission times. TOF is a function of both the speed of sound in air (primarily a function of temperature), and the air velocity that adds or subtracts to it in the path between the transceivers. While any variation in the speed of sound has the same impact on each of a pair's bidirectional TOF calculations, presence of air movement has an opposite effect. The TOF in the same direction of air flow experiences a decrease whereas the TOF in the opposite direction experiences an increase. Given the TOFs and the distance d between a pair of transceivers, air velocity is given by:

$$\overrightarrow{v_{a-b}} = 0.5\left(\frac{d}{TOF_{a-b}} - \frac{d}{TOF_{b-a}}\right) \quad (1)$$

Where $\overrightarrow{v_{a-b}}$ is the air velocity from transceiver a to b, d is the distance between transceivers a and b, and $TOF_{a-b}$is the time of flight from transceiver a to b. Speed of sound is also derived by (2).

$$c_{a-b} = 0.5\left(\frac{d}{TOF_{a-b}} + \frac{d}{TOF_{b-a}}\right) = \sqrt{\frac{\gamma kT}{m}} \cong 331.5 + 0.607T \quad (2)$$

Where c_{a-b} is the speed of sound between transceiver a and b, γ, k and m are air characteristic values (adiabatic index, Boltzmann constant, and molar mass), and T is the absolute temperature of the air. At 293K, the speed of sound is 343m/s and increases by 0.6m/s per degree Kelvin. Two sensors spaced at 0.1m will have a nominal TOF of 291.5µsec. Increasing the temperature by 1K will decrease the time of flight to approximately 290.9 µsec, a difference of 0.6 µsec. Adding 1m/s air velocity blowing from transceiver a to b will create a TOF of 290.7 µsec and a bidirectional TOF difference of 1.7µsec.

In order to generate strong resonant vibrations in the receiving transceiver, both communicating transceivers should have nearly identical natural frequencies (f_n). The MEMS membranes with integrated control electronics have natural frequencies matched to within 1kHz under controlled conditions (see Section 5). At power on, the transceiver measures the natural frequency of the membrane at the current moment. The transmitter's piezoelectric membrane (these ultrasonic devices are known as Piezoelectric Micromachined Ultrasonic Transducers (pMUT)) vibrates in response to the electrical input signal (Fig. 1a) and the mechanical motion of the membrane (Fig. 1b) causes the surrounding air molecules to vibrate at the transmitting frequency. The sound is emitted from the end of a resonant acoustic tube and spreads isotropically until it is received by a target receiver. Along the length of the path, the sound intensity is reduced by the spreading of the sound and by thermoviscous heating of air molecules. As the mechanical (acoustic) waves transfer energy onto the receiver's membrane, it begins to resonate with a similar frequency to the original electrical input signal (Fig. 1c).

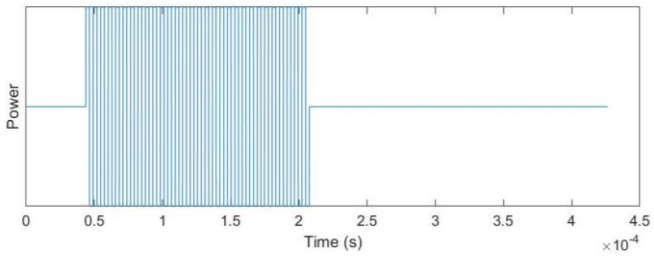

a) Alternating current with square waves at the natural frequency of transceiver.

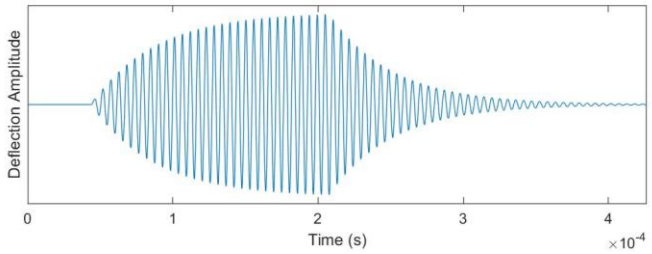

b) Transmitter's membrane vibrates in response to the exerted power, producing ultrasonic waves.

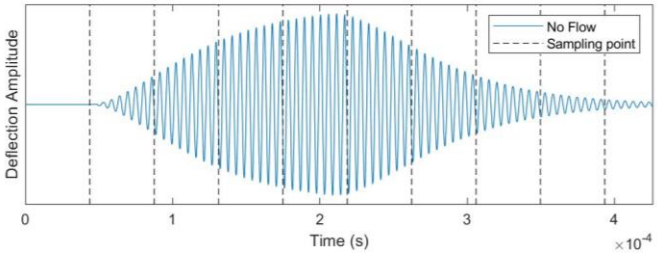

c) Receiver's membrane resonates with ultrasonic waves.

http://dx.doi.org/10.1109/JSEN.2019.2920648
https://escholarship.org/uc/item/8kf1c11k

Fig. 1. Pulsed signal transmission and reception.

The transceiver's application specific integrated circuit (ASIC) amplifies the signal produced by the pMUT and directly digitizes the signal at the ultrasonic frequency using a bandpass sigma-delta analog-to-digital converter. The digital output is then demodulated and filtered by a complex demodulator. The ASIC reports the in-phase (I_i) and the quadrature (Q_i) components at regular sampling intervals (i) which are spaced by $\frac{8}{f_n}$ or typically 45 µsec. The IQ samples can be used to calculate magnitude ($M_i = \sqrt{{I_i}^2 + {Q_i}^2}$) and phase ($\varphi_i = \tan^{-1}(I_i, Q_i)$).

As the ultrasound pulse arrives at the receiver, M_i increases until a maximum point, after which it decreases (Fig. 1c). In Fig. 2a, the ultrasonic waves are shown for a baseline condition in still air, and for another condition in which the pulse arrives earlier, with a reduced TOF. The early arrival could be due to an increase in the ambient speed of sound, as occurs with a rise in temperature, or to a downwind sound path, in which the speed of wind adds to the speed of sound.

The earlier the arrival, the more the phase angle φ_i of the received signal moves in a counter-clockwise direction (Fig. 2b). The envelope of the early arriving pulse is also shifted to the left.

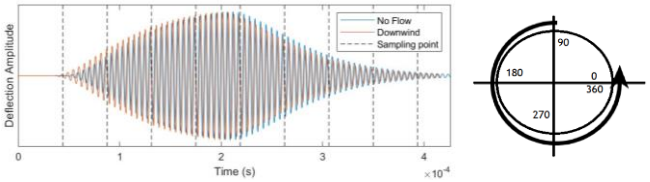

a b

Fig. 2a: Downwind impact on vibration in the receiver and signal magnitudes.
Fig. 2b: Counterclockwise phase rotation in the downwind flight path scenario (TOF reduction).

The wave pulse may alternatively arrive later at the receiver than the baseline, with an increased TOF (Fig. 3). The late arrival may be due to a decrease in the ambient speed of sound (e.g. drop in temperature) or to an upwind sound path. As the mechanical waves arrive later, the phase angle φ_i moves in the clockwise direction (Fig. 3a) and the envelope of the late arriving pulse is also shifted to the right.

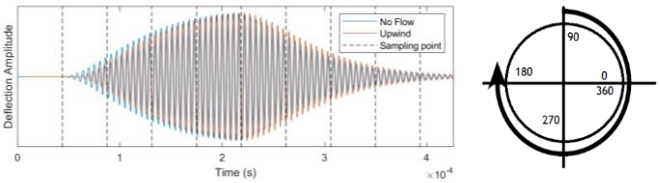

a b

Fig. 3a. Upwind impact on vibration in the receiver and signal magnitudes.
Fig. 3b: clockwise phase rotation in the upwind scenario (TOF increase).

All phase-difference methods use the phase difference among samples, the natural frequency of the membranes, and the reference TOF to calculate TOF (3).

$$TOF_t = TOF_{t-1} + (\varphi_t - \varphi_{t-1}) * \frac{1}{2\pi f_n} \quad (3)$$

The reference TOF can be calculated based on the distance between the two transceivers and the speed of sound (4).

$$TOF_0 = \frac{d}{c_0} \quad (4)$$

Where d is the distance between transceivers and c_0 is the speed of sound obtained during an initial calibration in still air.

If the airflow/temperature-induced phase difference is less than half a cycle (180°), the TOF difference is simply the difference between the current phase and preceding phase ($\Delta\varphi_{t,t-1}$) multiplied by $\frac{1}{2\pi f_n}$. This is used by the most prevalent algorithm in the literature [11], which limits the phase difference to $\frac{0.5}{f_n}$ (the current phase must be within a half cycle of the initial calibration phase (φ_0)). The maximum airflow/temperature range measurable by this method is calculated from (1). Greater than half a cycle, the challenge is to understand the directionality of phase measurements (since phase angles are limited to values between 0 to 360). To capture larger air velocities, the phase differences caused by both airflow and temperature variations would have to be capable of exceeding the half cycle limit. This might be accomplished by adding complementary algorithms and heuristics that track phase cycles or directly measure them.

III. Proposed Heuristic-Based Phase-Difference Methods

In this paper, we introduce and evaluate three heuristic-based methods: (1) Chained half-cycle-limit, (2) Magnitude-guided, (3) Temperature-guided. These methods can all be applied to pulse-wave methods. The chained half-cycle method and temperature-guided methods can also be used in continuous-wave methods of determining time of flight.

Each of these proposed phase-tracking methods determines the cumulative relative phase difference ($\Delta\varphi_{t,0}$), representing the total TOF difference between the initial calibration (4) and the current measurement.

A. Chained Half-cycle-limit Algorithm

This algorithm "chains" together phase measurements across wavelengths (cycles) by applying the within-a-half-cycle assumption to each preceding measurement (instead of to the initial measurement) and accumulating them. In this method, we assume that the phase shifts (clockwise and counter-clockwise rotation within 0-360 points) occur around the horizon with a freedom of rotation between 0-360 degrees, changing the wave cycle by at most one. When the phase wraps around in either clockwise or counter-clockwise directions, it enters the adjacent wavelength. The phase at time t (φ_t) is assumed to be within the half cycle around the phase at the time t – 1 (φ_{t-1}), and $|\varphi_t - \varphi_{t-1}| < 180°$ is used as a heuristic to determine the rotation direction. Two data filters are applied to

http://dx.doi.org/10.1109/JSEN.2019.2920648
https://escholarship.org/uc/item/8kf1c11k

buttress this assumption:

In the first filter, we drop any point within 50° of a 180° shift (outlier range in Fig. 4), to filter out samples that could cause the algorithm to lose track of the current TOF estimate. If we only attempt to find the closest rotation angle of an absolute phase to determine its relative phase, we may get undesired jumps in phase. For example, in a low air velocity situation we have a stream of absolute phases with a noise spike: -20, 10, 0, 20, -170, -20. A closest rotation interpretation would produce the relative phases -20, 10 (+30), 0 (-10), 20 (+20), 190 (+170), 340 (+150). The +170 and +150 relative phase difference total 320 which is a misinterpretation of a spike into a very sudden increase in the flow. Therefore, in the chaining algorithm, we reject all points within a certain number of degrees from 180. If we set this number at 50, then we would allow a maximum of 130-degree phase shift. Thus, the -170 point will be discarded as noise, and the following point -20 will be compared to the previous point 20, and thus be retained as data.

algorithm Chained half-cycle-limit algorithm **is**

input: phase at time t (φ_t)

in memory: phase at time t-1 (φ_{t-1}), relative phase at time t-1 ($\Delta\varphi_{t-1}$)

output: relative phase at time t ($\Delta\varphi_t$)

$\Delta\varphi_0 \leftarrow 0$

$d_t \leftarrow \varphi_t - \varphi_{t-1}$

if abs(d) > 180 **then**

$d_t \leftarrow -1 \times \text{sign}(d_t) \times (360 - \text{abs}(d_t))$

if !is_noise(φ_t) **then**

$\Delta\varphi_t \leftarrow \Delta\varphi_{t-1} + d_t$

Return $\Delta\varphi_t$

algorithm is_noise **is**

input: φ_t, d, outlier_range (LR), jerk_limit (JL)

in memory: φ_{t-1}, φ_{t-2}, d_{t-1}

output: Boolean (T)

$T \leftarrow$ False

if $180 - \text{abs}(d_t) \le LR$ or $\text{abs}(d_t - d_{t-1}) \ge JL$ **then**

$T \leftarrow$ True

Return T

Fig. 4. Pseudocode for chained half-cycle-limit algorithm

In the second filter, we drop any point where the change in phase differences between the next point and the current point, and the current point and the previous point, is greater than 120° (jerk_limit in Fig. 4). For example, using our outlier threshold of 50 degrees from the filter in 1 above, we consider a collection of consecutive relative phases in our stream 20, 140, -20, -40, etc., in which 140 is noise. Here our filter 1 would not deduce that 140 is noise and will then erroneously conclude that 140 is valid and -20 is noise and continue to assume the rest of the stream is noise until another point comes within (180-50) of 140. To address this, we must also look at the point after 140 to determine 140's validity. Specifically, if the phase difference between a point and its predecessor and its successor are large, and the predecessor and successor are close, then the current point is likely noise and can be rejected (see Fig. 4 for pseudocode of the algorithm).

The TOF is then calculated based on the calibration period phase and natural frequency as the phase changes with each successive measurement (Eq 3).

This algorithm is expected to work under scenarios in which the phase changes less than half a cycle (180°) between each successive measurement. At high measurement frequency (higher than 10 Hz), there are few physically plausible causes for a full-cycle jump within two measurements. However, at lower measurement frequencies, the phase difference due to air speed, change in speed of sound, or sudden change in the orientation of the anemometer might change by more than half a cycle and cause a permanent error in the $\Delta\varphi_t$. There is no automatic recovery from this error.

B. Magnitude-guided Algorithm

Our second algorithm uses the variable wave magnitude in pulses to assist detecting the cycle of the measured phase; to enable a wider measurement range exceeding the half-cycle limit. During the calibration period described above, we also measure magnitudes at the sampling point i ($M_{0,i}$) and the previous sampling point i-1 ($M_{0,i-1}$). For n wavelengths between sampling points i and i - 1, we define $waveMag$ as $\frac{M_{0,i}-M_{0,i-1}}{n}$. We use this to calculate the expected values of magnitudes ($EM_{t,j}$) of the observed phase (φ_t) at j wave numbers (j ∈ [-3, -2, -1, 0, 1, 2, 3]) on both sides of the initial calibration wave and then use brute-force search to find the j that minimizes $EM_{t,j} - M_t$.

We use j, φ_0, and φ_t to calculate $\Delta\varphi_t$ as shown in Fig. 5. By not having to constantly keep track of phase enables lower sampling rates and lowers the chance of incorrect phase estimations caused by sudden temperature or velocity changes that might shift the phase more than half a cycle at any sampling time t. The algorithm is presented in Fig. 5. The TOF is then calculated based on the calibration period TOF_0 and the derived $\Delta\varphi_t$ (Eq 3).

algorithm Magnitude guided algorithm **is**

input: phase at time t (φ_t), magnitude at time t (M_t),

wave magnitude ($waveMag$)

in memory: phase at time 0 (φ_0), magnitude at time 0 (M_0)

output: relative phase at time t ($\Delta\varphi_t$)

for each j ∈ [-3, -2, -1, 0, 1, 2, 3]

$EM_{t,j} \leftarrow M_0 + (j + \frac{\varphi_t - \varphi_0}{360}) \times waveMag$

$j_{min} \leftarrow$ index of $\min_j(EM_{t,j})$

$\Delta\varphi_t \leftarrow \varphi_t - \varphi_0 + j_{min} \times 360$

Return $\Delta\varphi_t$

Fig. 5. Pseudocode for magnitude-guided algorithm

This results from this algorithm might become noisy in extreme environmental conditions, since the vibration magnitude is impacted more than phase angle by changes in temperature and other external high-frequency vibration sources such as from scraping metal. Adding the magnitude

http://dx.doi.org/10.1109/JSEN.2019.2920648
https://escholarship.org/uc/item/8kf1c11k

value does however provide a mechanism for automatic recovery from error without needing recalibration in still air.

C. Temperature-guided Algorithm

The anemometer might be integrated with a physical temperature sensor positioned in the airstream. The measured temperature can guide a search for locating the cycle of the current phase angle relative to the calibration phase angle.

For a pair (a and b) of transceivers' calibration phases ($\varphi_{0,a-b}, \varphi_{0,b-a}$) and temperature ($T_0$), we use temperature at time t (T_t) to estimate the no-airflow phase for both paths at time t ($\varphi'_{t,a-b}, \varphi'_{t,b-a}$). The difference between the measured phases and the calculated no-airflow phases are due to the air speed, the difference in temperature measured by the sensor, and the temperature that actually impacts the pair's TOF.

We then distinguish what part of the phase difference comes from air speed, and what come from temperature differences. We correct our original estimate of phase difference ($\varphi'_{t,a-b}$, $\varphi'_{t,b-a}$) and calculate air-speed-induced phase differences ($\Delta\varphi^{AF}_{t,a-b}, \Delta\varphi^{T}_{t,a-b}, \Delta\varphi^{AF}_{t,b-a}, \Delta\varphi^{T}_{t,b-a}$), relying on the pragmatically based assumption that the airflow-induced TOF is smaller than half a cycle ($\frac{0.5}{f_n}$). Since phase differences from air speed are opposite for both directions and temperature differences are the same, the relative contributions can be separated by the method in Fig. 6.

The $\Delta\varphi_t$ required for (3) is then calculated as the sum of $\Delta\varphi^{AF}_{t,a-b}$ and $\Delta\varphi^{T}_{t,a-b}$ for path (a-b), and the sum of $\Delta\varphi^{AF}_{t,b-a}$ and $\Delta\varphi^{T}_{t,b-a}$ for the path (b-a).

The algorithm applies only to pairs of transceivers. The algorithm enables automatic correction of cycle determination errors without the need for a recalibration period in still air.

algorithm Temperature guided algorithm **is**

input: path 1 and 2 phase at time t ($\varphi_{t,a-b}, \varphi_{t,b-a}$), natural frequency ($f_n$)
temperature at time t (T_t), distance between pair (d_{a-b})
in memory: path 1 and 2 phase at time 0 ($\varphi_{0,a-b}, \varphi_{0,a-b}$)
temperature at time 0 (T_0)
output: path 1 and 2 relative phase at time t ($\Delta\varphi_{t,a-b}, \Delta\varphi_{t,b-a}$)

$dp_T \longleftarrow (\frac{d_{a-b}}{c(T_t)} - \frac{d_{a-b}}{c(T_0)}) \times \frac{360}{f_n}$
$\varphi'_{0,a-b} \longleftarrow (\varphi_{0,a-b} + dp_{temp}) \% 360$
$\varphi'_{0,b-a} \longleftarrow (\varphi_{0,b-a} + dp_{temp}) \% 360$
$dp_{a-b} \longleftarrow \varphi_{t,a-b} - \varphi'_{0,a-b} + \text{int.div } (\varphi_{t,a-b} - \varphi'_{0,a-b}, 180) \times -360$
$dp_{b-a} \longleftarrow \varphi_{t,b-a} - \varphi'_{0,b-a} + \text{int.div } (\varphi_{t,b-a} - \varphi'_{0,b-a}, 180) \times -360$
$\Delta\varphi_{t,a-b} \longleftarrow dp_T + \text{sign}(dp_{a-b}) \times dp_{a-b}$
$\Delta\varphi_{t,b-a} \longleftarrow dp_T + \text{sign}(dp_{b-a}) \times dp_{b-a}$
Return $\Delta\varphi_{t,a-b}$ & $\Delta\varphi_{t,b-a}$

Fig. 6. Pseudocode for temperature-guided algorithm

It should be noted that the maximum airspeed-induced TOF measurable by the temperature-guided method must be within a half phase cycle ($\frac{0.5}{f_n}$) neighborhood of the TOF in the still air calibration value corrected for temperature. The corresponding maximum upwind and downwind velocities possible for the anemometer can be derived from (5).

$$v_{\max} = c_0 - \frac{d}{\frac{d}{c_0} \pm \frac{0.5}{f_n}} \tag{5}$$

The maximum measurable velocity is thus an inverse function of the distance between the transceivers. At a natural frequency of 176 kHz, a distance between transceivers of 6 cm, and the speed of sound of 343 m/s, the maximum velocity would be +5.5 m/s, and -5.7 m/s. Lower natural frequencies would allow approximately linear increases in maximum measurable velocities.

IV. Reflection Induced Design Constraints

Any disturbances to the receiver before the time that I and Q values are measured for TOF calculations cause noise in the measurement. For example, if there is any surface close enough to the straight path between the two transceivers to reflect the ultrasonic waves, the receiver would experience overlapping waves that affect the membrane vibration and thus I and Q measurements. Both magnitude and phase outputs would then become noisy. Fig. 7 demonstrates the condition where reflections are received by the transceivers.

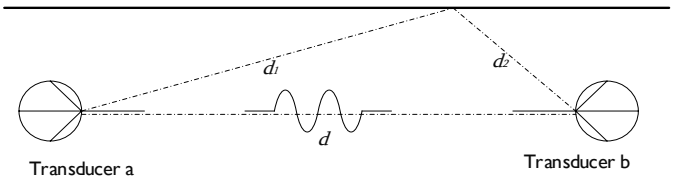

Fig. 7. Transceivers receiving reflections of a wall

As seen in Fig. 7, in order to eliminate reflections from surrounding surfaces, the distance between the sender, the closest reflective surface, and the receiver, should be greater than the distance from the sender to the receiver plus the distance traveled by any ultrasonic waves arriving at the I and Q measurement time. (6) demonstrates the described design constraint.

$$d + \frac{k}{f_n} \times c \leq d_1 + d_2 \tag{6}$$

In the current implementation, k is 30, the number of cycles of electric signal to the membrane within a pulse.

In another continuous-wave method using series pulses anemometer [7] reflections are actively suppressed by emitting an additional pulse with a 180° phase shift to cancel reflections. The reflection constraint also applies to continuous wave methods [8], [9], [15] where k can be considered infinity (the waves are constantly propagated by the sender and the receiver is continuously vibrating). In such cases the reflections can only be dealt with by reducing the strength of the reflected waves by soundproofing.

http://dx.doi.org/10.1109/JSEN.2019.2920648
https://escholarship.org/uc/item/8kf1c11k

V. Low Power MEMS Ultrasonic Transceivers

The transceiver used in this anemometer is a miniature, ultra-low power ultrasonic time-of-flight range sensor (CH101) from Chirp Microsystems. Based on AlN (Aluminum Nitride) piezoelectric MEMS technology [12]-[14], the CH-101 is a system-in-package that integrates a PMUT (piezoelectric micromachined ultrasonic transceiver) together with an ultra-low power SoC (system on chip) in a miniature, reflowable package. The SoC runs Chirp's ultrasonic Digital Signal Processing (DSP) algorithms and includes an integrated microcontroller that provides digital range readings via Inter-Integrated Circuit (I2C).

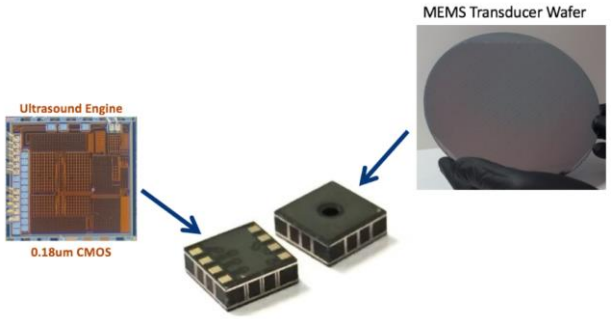

Fig. 8. The 3.5 mm square transceiver CH-101 made with MEMS processes on a silicon wafer. At the center of the photo, two sides of the CH-101 are shown; At left, the bottom of the Land Grid Array (LGA) package showing the 8 digital I/O pins; at right, the acoustic port where sound is emitted and received.

The Application Specific Integrated Circuit (ASIC) contained in CH-101 is connected to the MEMS piezoelectric membrane that vibrates at approximately 176 kHz. A similar ASIC is described in [14]. The system is designed to be triggered by a microcontroller such as the Microchip SAM-R21 on the carrier board such that all the CH-101 in the system can be synchronized to start transmitting or recording synchronously. The CH-101 has a digital interface, a 1 m maximum range, and power consumption in the range of 10uW-1mW depending on operating mode and sampling rate.

The CH-101 runs specialized firmware to control the operation of the sensor. This firmware is optimized for each application and loaded at run-time. The custom anemometry firmware controls the measurement process and permits the microcontroller to read out the IQ data. Each sending-receiving cycle requires about 10ms (to allow the ultrasound to decay to an undetectable level and avoid a pulse from the previous measurement being detected during the current measurement). Since each CH-101 in the system takes a turn transmitting, the full time to complete one measurement is N*10ms, where N is the number of CH-101s. Therefore, the maximum possible measurement rate is approximately 25Hz in systems with four CH-101. However, such frequency is not often needed for capturing variations in the real-world indoor air velocity environment.

The system in the following tests was triggered by a Microchip SAM-R21 at a measurement rate of 2 Hz. Raw IQ data was sent from the CH-101s in the system through the SAM-R21 to a PC which processed the signal from raw IQ data into air velocity estimates.

VI. Anemometer Testing

Transceivers were mounted on wands on opposite sides of a square-section wind tunnel, as shown in Fig. 9. They were separated by 16.5 cm and staggered at 17 degrees with respect to the direction of airflow. This was done to provide the necessary downwind distance and assure that the wake of the upwind sensor did not affect the airflow in the path between the transceivers. If we were to move one of the wands further downwind from the other wand, it increases the angle between the line connecting transducers and wind direction, and the sensor becomes more sensitive to variations in airspeeds. On the other hand, if the line connecting two transducers approaches perpendicular to the flow, the TOF and therefore airspeed become insensitive to changes in the airflow.

Fig 9. Experimental setup for our sensing systems in a duct

The airflow was provided by an EBM Papst axial fan (110V, 60 Hz, 95 W) with a max speed of 2380 rpm. An Optidrive E2 variable frequency drive controlled fan velocities across a range from 10%-100%. To provide a uniform flow with minimal turbulence, a bellmouth with 8cm deep stretch of honeycomb tubes to act as flow-straighteners (0.75cm cell width) was installed at the entrance to the duct. Traverses with a hot-wire anemometer (TSI Velocicalc Model 8345) assured that the flow across the test section was uniform. The TSI anemometer is rated to have an error of ± 3% of reading or 0.015 m/s whichever is greater. We calibrated the anemometer using a calibration wind tunnel paired with differential pressure sensor (Omega model WT4401-S). To ensure that the airflow in the tunnel is uniform, we measured airspeeds at 9 locations in a 3x3 mesh of the tunnel at a low speed (0.68 m/s) and a high speed (2.52 m/s). The standard deviation of measurements was 0.02 m/s for low speed and 0.05 m/s high speed, demonstrating uniform flow in the tunnel.

A series of air speeds was tested ranging from 0 m/s to 4 m/s, using a 0.25 m/s step below 1m/s and 0.5 m/s afterwards, all at 23°C. Each airflow rate period was set to 30 seconds intervals with at least 15 seconds of transition time between each step to allow the fan rotation to stabilize.

VII. Anemometer Performance

A. Velocity measurement

As seen in Fig. 1c, phase values are measured at different sampling points (i). For calculating TOFs, we measure the phase at sampling point i_{max} - 2 (located two points before the maximum magnitude sampling point). At a higher or lower

http://dx.doi.org/10.1109/JSEN.2019.2920648
https://escholarship.org/uc/item/8kf1c11k

point (e.g., i_{max} – 1 or i_{max} - 3) and under high temperature or air velocity changes, the sampling point may pass over the maximum magnitude and capture conditions incorrectly or move to lower indices which do not measure any of the transmitted signal.

Fig. 10 and 11 demonstrate the raw output signal out of the transceiver pair. The figures are color-coded to indicate associated air velocities measured by hot wire. Lower intensity blues are assigned to lower air speed measurements while higher intensity reds represent higher air speed measurements.

Fig. 10a shows data for a transceiver located upwind, showing a direct relationship between increasing airflow and magnitude. Fig. 10b shows the phase values rotating clockwise with increasing velocity (Fig. 3b). These calculated phase values closely match their associated air velocities even though the raw in-phase and quadrature components (Fig. 10c and d) do not by themselves predict the velocities well. In the downwind scenario of Fig. 11, magnitude values show noisy behavior. The phase values capture the associated velocities well, rotating counterclockwise with increased velocity. The raw in-phase and quadrature components again do not well represent the air velocity.

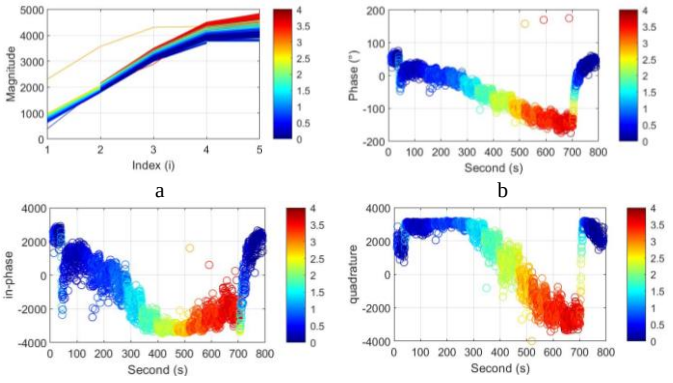

Fig. 10. Upwind transceiver measurements of magnitude, phase, in-phase, and quadrature values

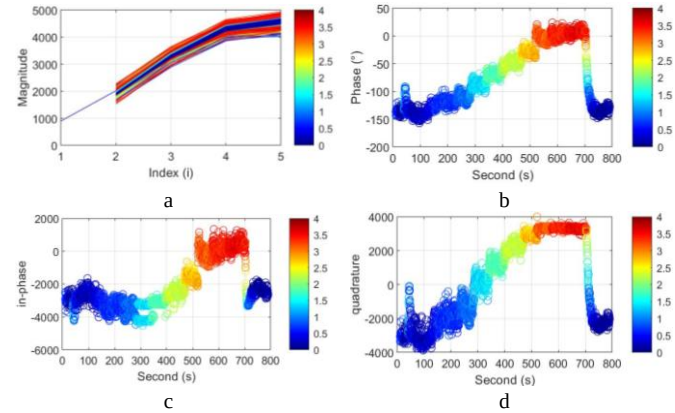

Fig. 11. Downwind measurements of the magnitude, phase, in-phase, and quadrature values

Fig. 12 and Fig. 13 show the calculated velocity and temperature results from our temperature guided phase tracking algorithm. We used 30-measurements to calibrate to zero velocity. The calculated air velocity is corrected for the cross-flow angle of the transmitter-receiver axis. The continuous, blue line is the calculated air velocity, and the horizontal red lines represent the mean air velocity measured within the 30 second intervals listed in Table 1. Some of the notable spikes are due to velocity overshoot in the wind tunnel as the variable frequency drive was manually adjusted in upward steps. The decrease in airflow starting from 690 seconds shows the fan winding down after it was turned off.

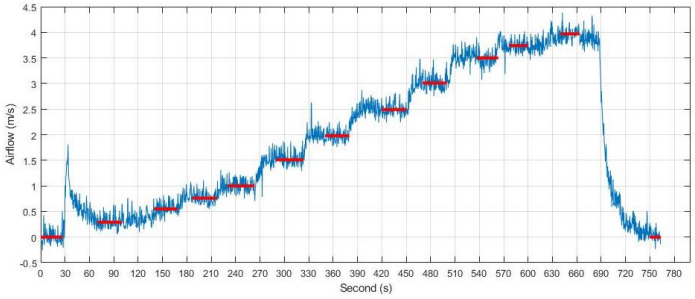

Fig. 12. Calculated airflow from phase tracking algorithms.

The calculated sonic temperature is shown in Fig. 13. Its relative values remained within narrow limits during the period of the experiment with its increasing velocities. The figure shows a consistent but unexplained effect of air velocity on the transceivers used in the anemometer, indicating an imaginary temperature drop of 0.8K when the velocity rises above, or falls below, a still air threshold (~0.2m/s). It comes from our associating the shift in the mean of a transceiver pair's TOFs to temperature alone. These results suggest that there are other factors impacting the transceivers in creating bidirectional TOF shifts.

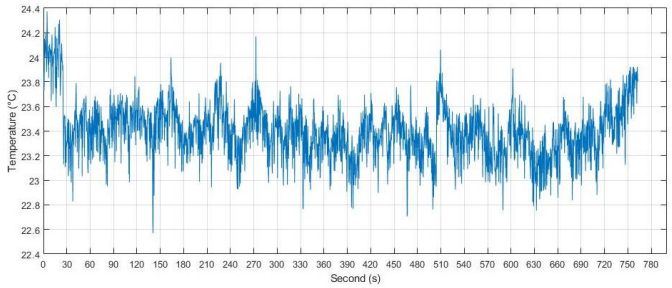

Fig. 13. Measured air temperatures from adaptive phase tracking algorithms.

B. Error measurement

In order to assess the performance of the sensing device to capture airflow rates accurately, we used two goodness-of-fit measures, namely, root mean square (RMS) and mean absolute error (MAE). (7) and (8) demonstrates the procedure to calculate the measures.

$$RMS = \sqrt{\frac{1}{n}\sum_{i=1}^{n}\left(c_{c,i} - c_{m,i}\right)^2} \tag{7}$$

$$MAE = \frac{1}{n}\sum_{i=1}^{n}\left|c_{c,i} - c_{m,i}\right| \tag{8}$$

Where n is the number of data points in the data set of airflow measurements, i is the time index in which the airflow rates were measured, $c_{c,i}$ is the measured airflow from the adaptive

http://dx.doi.org/10.1109/JSEN.2019.2920648
https://escholarship.org/uc/item/8kf1c11k

phase algorithm, and $c_{m,i}$ is the exact value airflow measurement.

Table 1 demonstrates the goodness of fit results based on the 30 seconds fixed airflow measurements (red lines in Fig. 12). Uniform goodness of fit measures was observed over all air velocities with no specific bias towards a specific velocity. The average unfiltered RMS velocity noise was 0.1294 m/s and the MAE error was 0.0542 m/s. The mean measurements were also very close to mean measured airflow rates.

Table I
Airflow rates at each calibration period

	Measured airflow (m/s)	Mean measurements (m/s)	Root Mean Square	Mean Absolute Error (m/s)
	0	0.01	0.14	0.2
	0.28	0.29	0.13	0.03
	0.53	0.53	0.14	0.04
	0.76	0.77	0.12	0.03
	1.00	1.00	0.12	0.05
	1.51	1.53	0.14	0.06
	1.98	1.97	0.12	0.06
	2.49	2.49	0.12	0.06
	3.01	3.02	0.15	0.06
	3.50	3.49	0.16	0.06
	3.74	3.74	0.12	0.01
	3.97	3.97	0.12	0.03
	0.02	0.04	0.10	0.02
Mean goodness of fit			**0.13**	**0.05**

C. *Filter rate – Accuracy Trade-off*

In order to reduce noise, any type of low-pass model free filter could be applied to the measurements. Here we used the Savitzky-Golay filter which reduces noise by convolution, applying linear least squares to adjacent points to generate polynomials predicting the smoothest successive point. The filter produces a smoother curve with limited dramatic peaks and valleys, making for a clearer data set. We fixed the polynomial order to 1 and varied the measurement window (frame length). Fig. 14 demonstrates the results for both goodness of fit measures. The optimum frame length for both measures was between 10 and 20. Considering the direct relation between a lower frame length with a faster response time, we chose the frame length of 15 (with mean absolute error of 0.0263) rather than 18 (with mean absolute error of 0.0258). Fig. 15 demonstrates the filtered results based on the frame length of 15.

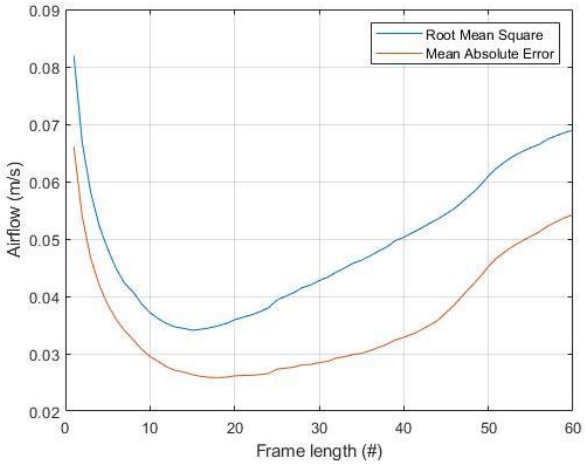

Fig. 14. Goodness of fit measures for different frame lengths of order 1 Savitzky-Golay filter

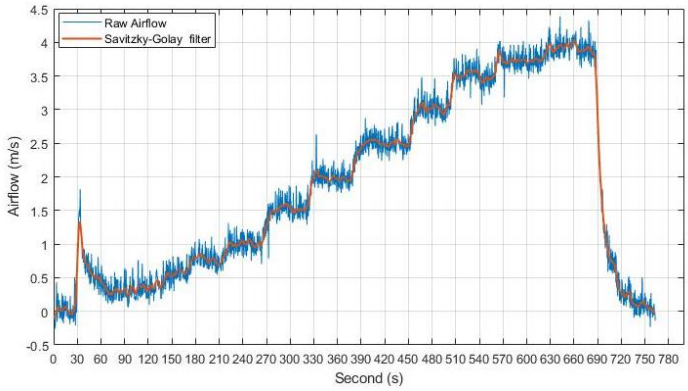

Fig. 15. Filtered airflow rates from order 1 Savitzky-Golay filter with frame length of 15

VIII. Discussion And Future Research

In summary, three algorithms are proposed for increasing the range and reliability of air velocity and temperature detection using a high-frequency pulsed-wave anemometer.

A new *chained-half-cycle method* works under scenarios in which the phase changes less than half a cycle (180°) between each successive measurement point. Chaining sequential measurements increases the range of velocities addressable by the anemometer. However, at lower measurement frequencies appropriate for indoor anemometry (less than 10 Hz), plausible abrupt changes in air velocity, speed of sound, or physical displacement of the anemometer) might produce a phase difference that exceeds half a cycle and causes a permanent error in the $\Delta\varphi_t$. This error is not automatically recoverable.

The *magnitude-guided* algorithm produces imperfect results in our system due to inconsistencies (relative to Fig. 2a and 3a) in the magnitude measurements from the transceivers in our system. However, this algorithm ideally has none of the half-cycle limitations that other methods have. It would work for systems with well-behaved magnitude measurements and auto-recover from phase difference errors. We are currently exploring the inconsistencies in our sensors' magnitude measurements.

The *temperature-guided* algorithm is reliable at capturing

http://dx.doi.org/10.1109/JSEN.2019.2920648
https://escholarship.org/uc/item/8kf1c11k

large phase differences caused by large changes in air velocity, temperature, or both. This method requires a temperature sensor within the measured air flow. Since the temperature measurements are only used to guide the search to find the phase cycle, they can be moderately noisy (± 2K for our sensing system). In flows with highly non-uniform temperatures, differences between the average temperature of the transceiver path and the temperature sensor reading will cause incorrect velocity calculation, but it will recover and work properly once non-uniformity subsides.

It should be noted that ultrasonic anemometers capture the average speed across the paths connecting transceivers. This serves to capture the volumetric air flow in ducts. However, they are not capable of measuring air speeds at a single point similar to hot wire anemometers. In addition, if the airflow in the tunnel has velocity components perpendicular to the tunnel direction, the ultrasonic device measurements become invalid. This may happen downstream of air duct elbows.

In this paper, we have focused on the calculation of TOFs for a single pair of transducers. This sensing system can be used in air ducts for measuring average speed passing through the cross-section of a duct. However, various formations of the transducers can also obtain 2D and 3D measurements of air velocity and volumetric air flow. The ability to monitor indoor air velocity enables various applications such as monitoring personal exposure to fresh air [15] and thermal comfort [16], [17]. It should only be noted that the time it takes to reach the required level of vibrations in the receiver to calculate TOF measurements must be greater than the time it takes for a reflection wave from any surrounding surface to arrive to the receiver. As a part of a future study, we are building 3-dimensional air velocity measurements using 4 transceivers in tetrahedron formation. This enables design of sensing devices that monitor personal environmental conditions and advanced control strategies [18], [19] to integrate into control loop of air conditioning systems for increased energy efficiency and occupants' comfort [20]-[22].

IX. Conclusions

To increase the limited air velocity range possible in high frequency phase-based ultrasonic anemometers, we developed new time-of-flight calculation methods that surpass the half-cycle limit used in existing phase-based calculations. Three approaches are presented to extend the range. We validated our final method with a very high frequency anemometer using MEMS ultrasonic transceivers containing an AlN piezoelectric micromachined ultrasound transceiver. Our results demonstrate high goodness of fit (average room mean square of 0.1294 m/s and the average mean absolute error of 0.0542 m/s) for capturing actual air velocities in the experimental setup. With a filter rate of 15 frame lengths in the filter, an absolute error of 0.0263 m/s was calculated, surpassing the sensitivity of many current commercially available products. The implementation of our sensing system requires very low power compared to continuous wave ultrasonic anemometers and is less expensive than existing sensors of comparable precision and durability. The anemometer's capabilities enable numerous opportunities to better manage environmental quality and reduce the energy required to condition the indoors.

References

[1] (January 31, 2019). *Anemometer*. *Available at "https://en.wikipedia.org/w/index.php?title=Anemometer&oldid=881065278"* .

[2] A. A. Quaranta *et al*, "A microprocessor based, three axes, ultrasonic anemometer," *Journal of Physics E: Scientific Instruments*, vol. 18, *(5)*, pp. 384, 1985.

[3] H. Dong and Y. Jun, "High accuracy time of flight measurement for ultrasonic anemometer applications," in *Instrumentation, Measurement, Computer, Communication and Control (IMCCC), 2013 Third International Conference on*, 2013, .

[4] J. Jin and H. TANG, "Design of Ultrasonic Wind Velocity Measurement System Based on ARM [J]," *Instrument Technique and Sensor*, vol. 6, pp. 101-104, 2009.

[5] D. Fernandes, L. Gomes and A. Costa, "Wind speed and direction measurement based on time of flight ultrasonic anemometer," in *Industrial Electronics (ISIE), 2017 IEEE 26th International Symposium on*, 2017, .

[6] V. P. Yadav, A. Sinha and A. Khosla, "Design and implementation of ultrasonic anemometer," in *Power, Control & Embedded Systems (ICPCES), 2017 4th International Conference on*, 2017, .

[7] A. Raine *et al*, "Development of an ultrasonic airflow measurement device for ducted air," *Sensors*, vol. 15, *(5)*, pp. 10705-10722, 2015.

[8] C. Yu *et al*, "Ultrasonic Wind Velocity Measurement Based on Phase Discrimination Technique," *Indonesian Journal of Electrical Engineering and Computer Science*, vol. 10, *(6)*, pp. 1157-1162, 2012.

[9] D. Han, S. Kim and S. Park, "Two-dimensional ultrasonic anemometer using the directivity angle of an ultrasonic sensor," *Microelectron. J.*, vol. 39, *(10)*, pp. 1195-1199, 2008.

[10] D. Xi-Bo *et al*, "Study of the ultrasonic three-dimensional wind speed measurement methods based on the phase difference," in *Instrumentation & Measurement, Computer, Communication and Control (IMCCC), 2016 Sixth International Conference on*, 2016, .

[11] D. Han and S. Park, "Measurement range expansion of continuous wave ultrasonic anemometer," *Measurement*, vol. 44, *(10)*, pp. 1909-1914, 2011.

[12] R. J. Przybyla *et al*, "3D ultrasonic rangefinder on a chip," *IEEE J Solid State Circuits*, vol. 50, *(1)*, pp. 320-334, 2015.

[13] R. J. Przybyla *et al*, "In-air rangefinding with an aln piezoelectric micromachined ultrasound transducer," *IEEE Sensors Journal*, vol. 11, *(11)*, pp. 2690-2697, 2011.

[14] S. Shelton *et al*, "CMOS-compatible AlN piezoelectric micromachined ultrasonic transducers," in *2009 Ieee International Ultrasonics Symposium*, 2009, .

[15] A. Ghahramani *et al*, "Personal CO2 bubble: Context-dependent variations and wearable sensors usability," *Journal of Building Engineering*, vol. 22, pp. 295-304, 2019.

http://dx.doi.org/10.1109/JSEN.2019.2920648
https://escholarship.org/uc/item/8kf1c11k

[16] A. Ghahramani *et al*, "Infrared thermography of human face for monitoring thermoregulation performance and estimating personal thermal comfort," *Build. Environ.*, vol. 109, pp. 1-11, 2016.

[17] A. Ghahramani *et al*, "Towards unsupervised learning of thermal comfort using infrared thermography," *Appl. Energy*, vol. 211, pp. 41-49, 2018.

[18] A. Ghahramani, K. Dutta and B. Becerik-Gerber, "Energy trade off analysis of optimized daily temperature setpoints," *Journal of Building Engineering*, vol. 19, pp. 584-591, 2018.

[19] A. Ghahramani, S. A. Karvigh and B. Becerik-Gerber, "HVAC system energy optimization using an adaptive hybrid metaheuristic," *Energy Build.*, vol. 152, pp. 149-161, 2017.

[20] A. Ghahramani, C. Tang and B. Becerik-Gerber, "An online learning approach for quantifying personalized thermal comfort via adaptive stochastic modeling," *Build. Environ.*, vol. 92, pp. 86-96, 2015.

[21] A. Ghahramani, F. Jazizadeh and B. Becerik-Gerber, "A knowledge based approach for selecting energy-aware and comfort-driven HVAC temperature set points," *Energy Build.*, vol. 85, pp. 536-548, 2014.

[22] A. Ghahramani *et al*, "Energy savings from temperature setpoints and deadband: Quantifying the influence of building and system properties on savings," *Appl. Energy*, vol. 165, pp. 930-942, 2016.

Ali Ghahramani received the B.S. degree in civil engineering from Shiraz University, Iran, in 2011 and he also received the M.Sc. degrees in civil and environmental engineering (2014), computer science (2016), and industrial and system engineering (2016), and the Ph.D. degree in civil engineering (2017) all from University of Southern California, Los Angeles, CA.

He is currently a Postdoctoral scholar and Lecturer at the Center for the Built Environment at UC Berkeley.

His research interests are in the areas of sensing, adaptive learning, and optimization systems that are specifically tailored for human-centered smart, resilient, and sustainable civil infrastructures. Non-intrusive sensing methods such as infrared thermography and ultrasound-based sensing, adaptive learning of human behaviors in buildings, statistical methods and machine learning for occupant-building large datasets, and optimal operation of human-in-the-loop building systems are among his research interests.

Megan Zhu is a 2018 graduate from UC Berkeley with a B.A. in Computer Science. She now works at Riot Games as an Associate Software Engineer on a Research & Development team.

Richard J. Przybyla received the Honors B.S. degree in electrical engineering from Oregon State University in 2008. In 2013, he earned a Ph.D. in electrical engineering from the University of California, Berkeley, where he and his colleagues demonstrated an ultrasonic 3D rangefinder system which fits on a chip.

In 2013, Richie co-founded Chirp Microsystems to commercialize his Ph.D. research, where he holds the position of System Architect. In 2018, Chirp Microsystems was acquired by TDK Corporation, a global leader in sensor technology and electronic components. Richard has also held R&D positions at Hewlett-Packard and Oregon State University. In 2019, he was inducted into the Oregon State Council of Outstanding Early Career Engineers. Richard is interested in circuits, algorithms, and systems which interface to the physical world.

Michael P. Andersen is completing his PhD in Electrical Engineering and Computer Science at the University of California in the prestigious RISELab under Dr. David Culler. His research covers wireless sensor networks, time series databases, operating systems for the built environment and secure communication infrastructure.

Parson J. Galicia is a second-year student at the University of California Berkeley pursuing his B.S. degree in Civil and Environmental Engineering. His academic interests revolve around environmentally sustainable engineering systems and smart civil infrastructures. He is currently the Jr. Vice President of External Affairs for the Berkeley Student Chapter of the American Society of Civil Engineers.

Therese Peffer earned her Ph.D. in Architecture with an emphasis on building science at UC Berkeley, a master's degree in Architecture at the University of Oregon, and a B.A. in neurobiology and psychology from UC Berkeley.

She is the Associate Director at California Institute for Energy and Environment (CIEE), along with the Program Director, Enabling Technology Development at CIEE, and Associate Director, CITRIS Sustainable Infrastructures Initiative. For the past five years she has co-chaired the annual Behavior Energy and Climate Change conference. Therese enjoys working with and managing multidisciplinary teams to "decarbonize comfort": improve building performance and thermal comfort while reducing energy consumption. Her research projects range from developing sensors, designing a thermostat for low income households, increasing usability of interfaces, improving control algorithms for heating and cooling systems in residential and commercial buildings, developing a virtual building automation system with networked sensors, thermostats, and energy meters for improved demand response and energy efficiency, and other smart grid and building-to-grid research projects.

Hui Zheng, PhD is a researcher at the Center for the Built Environment at UC Berkeley. She received her MS in Architecture in 1986, and BA in Engineering in 1983 from Tsinghua University, China. She holds a PhD in Building Science from the Department of Architecture at UC Berkeley. Her work focuses on efficient ways to achieve thermal comfort, and thermal comfort modeling in complex environments.

Edward Arens is Professor of the Graduate School, University of California Berkeley. His PhD is from the University of Edinburgh, in Architectural Science. He headed the Architectural Research Section at the National Bureau of Standards before coming to Berkeley in 1980. He is the founding Director of the Center for the Built Environment. His research interests address energy and environmental quality in the built environment, most recently by developing personal comfort systems, and technologies and standards enabling the use of air movement for efficiently cooling building occupants.

http://dx.doi.org/10.1109/JSEN.2019.2920648
https://escholarship.org/uc/item/8kf1c11k